Thermal radiation of di-tert-butyl peroxide pool fires—Experimental investigation and CFD simulation

Hyunjoo Chun[a], Klaus-Dieter Wehrstedt[b], Iris Vela[c], Axel Schönbucher[c,*]

[a] *Umicore Korea Limited, 410 Chaam-dong, Cheonan-city, Chungnam, 330-200, Republic of Korea*
[b] *Federal Institute for Materials Research and Testing (BAM), Working Group "Explosive Substances of Chemical Industries",*
Unter den Eichen 87, D-12205 Berlin, Germany
[c] *University of Duisburg-Essen, Institute for Chemical Engineering I, Universitätsstraße 5, D-45141 Essen, Germany*

ARTICLE INFO

ABSTRACT

Instantaneous and time averaged flame temperatures $\bar{T}$, surface emissive power $\overline{SEP}$ and time averaged irradiances $\bar{E}$ of di-tert-butyl peroxide (DTBP) pool fires with $d = 1.12$ and 3.4 m are investigated experimentally and by CFD simulation. Predicted centerline temperature profiles for $d = 1.12$ m are in good agreement with the experimental emission temperature profiles for $x/d > 0.9$. For $d = 3.4$ m the CFD predicted maximum centerline temperature at $x/d = 1.4$ is 1440 K whereas the emission temperature experimentally determined from thermograms at $x/d \approx 1.3$ is 1560 K. The predicted surface emissive power for $d = 1.12$ m is 115 kW/m² in comparison to the measured surface emissive power of 130 kW/m² whereas for $d = 3.4$ m these values are 180 and 250 kW/m². The predicted distance dependent irradiances agree well with the measured irradiances.

1. Introduction

A pool fire can occur when a flammable liquid is accidentally released on land or water and ignites. Buoyancy driven turbulent non-premixed flame is formed above the pool with a very small initial momentum of vaporized fuel.

Accidental pool fires can happen in the process industries [1] and during the transport or storage of hazardous burning substances [2–8]. Some publications about hydrocarbon pool fires [4,7,9–16,22–29] exist, whereas only a very small number of papers can be found about organic peroxide pool fires [6,17–21].

Some knowledge of much higher thermal radiation of organic peroxide pool fires exists [21], compared with those of the hydrocarbon pool fires. The hazards mostly result from their high thermal radiation which therefore demands a high control of the storage equipment [6]. A detailed knowledge of the thermal hazards of organic peroxide pool fires is therefore of great interest on the safety prevention in the process industries.

Thermal instability and high reactivity of organic peroxides come from their molecular structure contains relatively unstable –O–O– peroxy bonds [21]. In comparison with other organic perox-

ides, DTBP is thermally relatively stable and its fire has a low soot production.

To get values and prediction of flame temperatures (T), surface emissive power (SEP) and irradiances (E) depending on pool diameter, DTBP pool fires are investigated and results are presented in this paper.

SEP is usually defined as the heat flux due to thermal radiation at the surface area of the flame [29]. Several semi-empirical thermal radiation models are used to calculate the SEP of large fires: the point source model (PSM) [3–5,7,20,29], the solid flame model (SFM) [3–5,7,20,29,30] and the new organized structures radiation models (OSRAMO II, III) [3,7,20,24].

To determine the key parameter the time averaged surface emissive power $\overline{SEP}$ of a flame, also the flame surface $\overline{A_F}$ should be known [7,24–29]:

$$\overline{SEP}(d) = \bar{f}_{rad}(d) \frac{\bar{\dot{Q}}_c}{\overline{A_F}} \tag{1a}$$

with

$$\bar{\dot{Q}}_c = \overline{\dot{m}_f''}(-\Delta h_c)A_{pool} \tag{1b}$$

The time averaged $\overline{A_F}$ is determined from the instantaneous area A_F which is influenced by e.g. the flame fluctuations.

Most of semi-empirical radiation models use uniform $\overline{SEP}$ value over the whole flame surface $\overline{A_F}$ assuming flame to be a grey

* Corresponding author. Tel.: +49 201 183 3807; fax: +49 201 183 4196.
E-mail address: axel.schoenbucher@uni-due.de (A. Schönbucher).

Nomenclature

a_{hs}	area fraction of hot spots
a_{sp}	area fraction of soot parcels
a_x	area of a pixel, matrix element, in the thermographic image (m^2)
A	area (m^2)
A_F	flame area (m^2)
$\overline{A_F}$	time averaged flame area (m^2)
A_{pool}	pool area (m^2)
d	pool diameter (m)
dA	infinitesimal area (m^2)
dG	infinitesimal incident radiation (kW/m^2)
ds	infinitesimal distance (m)
dV	infinitesimal volume (m^3)
E	irradiance (kW/m^2)
f_{rad}	radiative fraction
$f_{m,s}$	soot mass fraction
$f_{v,s}$	soot volume fraction
G	incident radiation (kW/m^2)
h_{rim}	height of the pool rim (m)
Δh_c	specific heat of combustion (kJ/kg)
I	radiation intensity $(kW/(m^2\,sr))$
I_B	blackbody radiation intensity at temperature T $(kW/(m^2\,sr))$
k	absorption coefficient of the flame (1/m)
k_g	absorption coefficient of the flame gas mixture (1/m)
$k_{m,s}$	absorption coefficient of soot (1/m)
$\dot{m}_f$	mass flow rate of the fuel (kg/s)
$\dot{m}_f''$	mass burning rate of the fuel $(kg/(m^2\,s))$
N_T	number of total images in the thermographic sequence
p_a	ambient pressure (bar)
$\bar{\dot{Q}}_c$	heat of combustion (kW)
SEP	surface emissive power (kW/m^2)
SEP_{act}	actual surface emissive power (kW/m^2)
SEP_{hs}	surface emissive power of hot spots (kW/m^2)
$SEP_{i,j}$	local emissive power of a pixel element (kW/m^2)
SEP_{LS}	surface emissive power of luminous spots (kW/m^2)
SEP_{sp}	surface emissive power of soot parcels (kW/m^2)
SEP_{SZ}	surface emissive power of soot zones (kW/m^2)
t	time (s)
t_b	burning time (s)
Δt	time interval (s)
T	emission temperature (K)
T_a	ambient temperature (K)
$T_{i,j}$	temperature of the pixel element (K)
T_{in}	inlet temperature (K)
T_{max}	centerline maximum emission temperature (K)
x	axial coordinate in vertical direction (m)
y	radial coordinate in horizontal direction (m)
Δy	horizontal distance from the pool rim (m)
$\Delta y/d$	relative horizontal distance from the pool rim

Greek letters

α	absorbance of the receiving area element
β_F, β_E	view angles referring to a flame element, receiver element (°)
Ω	solid angle (sr)
σ	Stephan Boltzman constant $(5.67 \times 10^{-8}\ W/(m^2\,K^4))$
ε_F	flame emissivity
φ	view factor
ρ_a	density of air (kg/m^3)
ρ_f	density of fuel (kg/m^3)
ρ_s	density of soot (kg/m^3)
τ	atmospheric transmittance

Indices

a	ambient
act	actual
B	black body
exp	experiment
f	fuel
F	flame
g	gas
hs	hot spots
i, j	the position of the pixel element in thermogram
LS	luminous spots
m	mass
max	maximum
p	pressure
s	soot
sp	soot parcels
SZ	soot zones
T	temperature
$(^{--})$	time averaged value
$\langle\ \rangle$	spatial averaged values
max(a,b)	maximum of a and b
i, j	the position of the pixel element in thermogram
OSRAMO	organized structures radiation model
pdf	probability density function
s	direction of propagation
S-VHS	super high-speed video camera system

body [29]. Mudan [4] calculates actual $\overline{SEP}_{act}(d)$ averaged over the flame surface based on constant $\overline{SEP}$ values of luminous spots ($\overline{SEP}_{LS} = 140\ kW/m^2$) and soot zones ($\overline{SEP}_{SZ} = 20\ kW/m^2$). Schönbucher and coworkers [7] developed organized structures radiation models OSRAMO II, III validated for smoky pool fires. In OSRAMO II the $\overline{SEP}_{act}(d)$ is calculated based on hot spots ($\overline{SEP}_{hs}(d)$) and soot parcels ($\overline{SEP}_{sp}(d)$) and their area fractions $\bar{a}_{hs}(d)$ and $\bar{a}_{sp}(d)$:

$$\overline{SEP}_{act}(d) = \bar{a}_{hs}(d)\overline{SEP}_{hs}(d) + \bar{a}_{sp}(d)\overline{SEP}_{sp}(d) \tag{2}$$

In OSRAMO III [7] $\overline{SEP}_{act}(d)$ is determined based on pdf distributions of hot spots and soot parcels.

In this study an actual method is used to determine emission temperatures T and the surface emissive power SEP of DTBP and kerosene pool fires (d = 1.12 and 3.4 m) by evaluation of thermograms obtained by a thermographic camera which receives a thermal radiation from the fire [20,22–24].

The heat flux from a flame which can be received by e.g. radiometer, at a certain distance from the flame is defined as irradiance E [29]. The time averaged irradiances as a function of a relative distance $\Delta y/d$ can be calculated as [7]:

$$\bar{E}(\Delta y/d) = \tau \alpha \varphi(\Delta y/d)\overline{SEP}(d) \tag{3}$$

where $\varphi = f(\bar{A}_F, \Delta y/d, \beta_F, \beta_E)$ is the view factor, α is the absorbance of the receiver area element [31], and τ is an atmospheric transmittance.

The CFD simulation of large-scale hydrocarbon pool fires is under developing [7,24,30,32–39] and CFD of organic peroxide pool fires is almost unknown.

Table 1
Specifications of the thermographic camera.

Model	ThermaCAM™ Researcher
Detector type	Patented, uncooled microbolometer 640 × 480 pixel
Spectral range	7.5–13 μm
Thermal sensitivity	0.08 °C at 30 °C, Standard 50 Hz
Geometric resolution (IFOV)	1.3 mrad
Field of view (FOV)	24° × 18°/0.3 m (local width 35 mm)
Measurement range	40–1500 °C, to 2000 °C (option)
Accuracy	±2 °C, ±2% from the measured value
Digital output	14-bit real-time serial digital video

Table 2
Some important properties of DTBP gas phase, implemented in ANSYS CFX-11 code.

Di-tert-butyl peroxide (DTBP)	
Thermodynamic state	Ideal gas
Absorption coefficient	1 [1/m]
Dynamic viscosity	1.20×10^{-7} [kg/(m s)]
Molar mass	146 [kg/kmol]
Refractive index	1.3
Thermal conductivity	0.02 [W/(m K)]
Specific heat capacity	6.85
	$(17.34 + 0.72T - 3.36 \times 10^{-4}T^2 + 4.85 \times 10^{-8}T^3)$ [J/(kg K)]
Reference pressure	1 [bar]
Specific enthalpy of combustion	-1.78×10^7 [J/kg]

2. Experiments

Large-scale experiments with DTBP and kerosene pool fires $d = 1.12$ and 3.4 m have been carried out on the open air BAM Test-site Technical Safety (in Horstwalde, south of Berlin). Square shaped steel trays are used with the rim height of 0.08 m [20]. The fuel layer had a thickness of 0.05 m.

Emission temperatures are measured using a thermographic camera (ThermaCAM™ Researcher). In Table 1, the technical specifications of the thermographic camera are presented. For the emissivity $\varepsilon_F(d)$ of hydrocarbon pool fires the following values are used: $\varepsilon_F(d = 1.12\,m) = 0.95$, $\varepsilon_F(d = 3.4\,m) = 0.98$ [22,29,40]. These emissivity values were adopted for the DTBP pool fires because in regard to the dependence of emissivity on the optically thickness of a flame the distinction between a hydrocarbon flame and a DTBP flame is low.

Ellipsoidal radiometers with wide angle are used to measure the irradiances $E(\Delta y)$ from the fire as a function of the horizontal distance Δy [20].

3. CFD simulation

In the computational fluid dynamics (CFD) simulation of DTBP pool fires (Table 2) a domain consists, in this study of three dimensional rectangular hexahedral unstructured mesh with dimensions of 10 m × 10 m × 10 m for $d = 1.12$ m and of 20 m × 20 m × 30 m for $d = 3.4$ m (Fig. 1). The domain contains air at ambient conditions: $T_a = 293$ K and $p_a = 1.013$ bar. The fuel source is defined as an inlet boundary with a constant temperature $T_{in} = 373$ K and a constant mass flow rate $\bar{\dot{m}}_f$ ($\bar{\dot{m}}_{DTBP}$ ($d = 1.12$ m) = 0.28 kg/s and $\bar{\dot{m}}_{DTBP}$
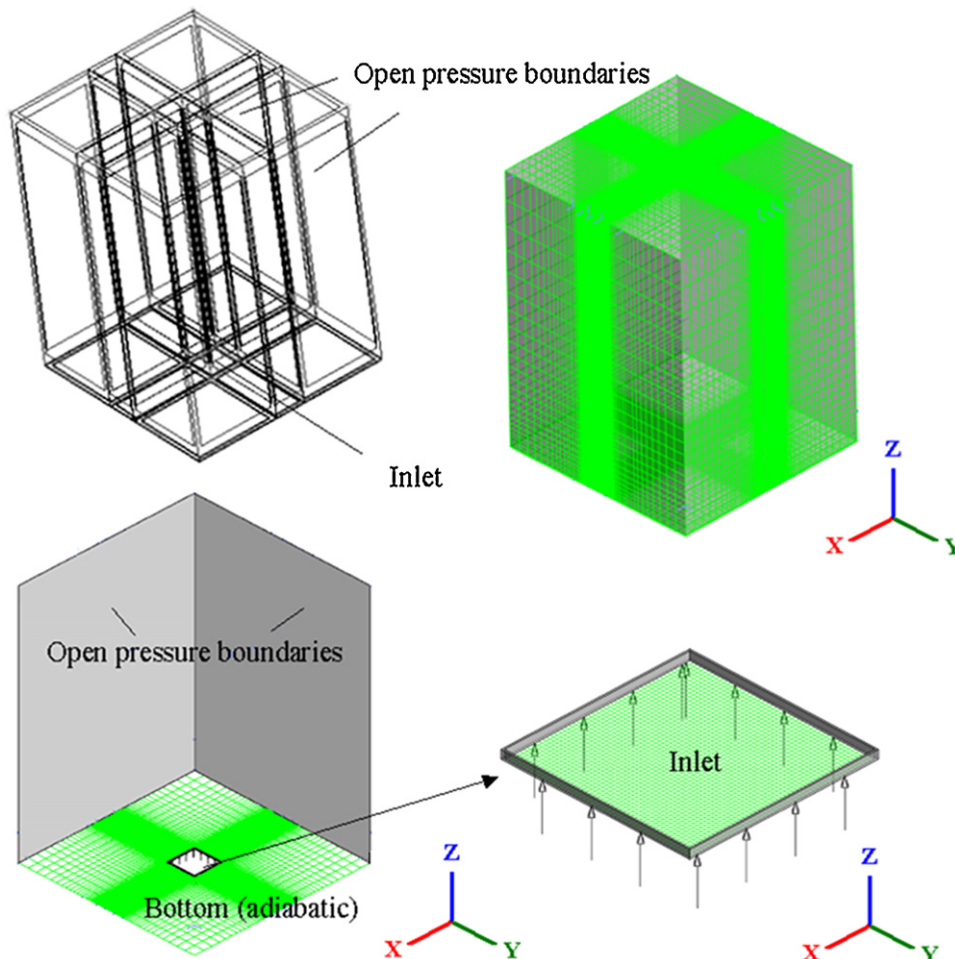

Fig. 1. Computational domain and the boundary conditions for the CFD simulation of DTBP pool fires.
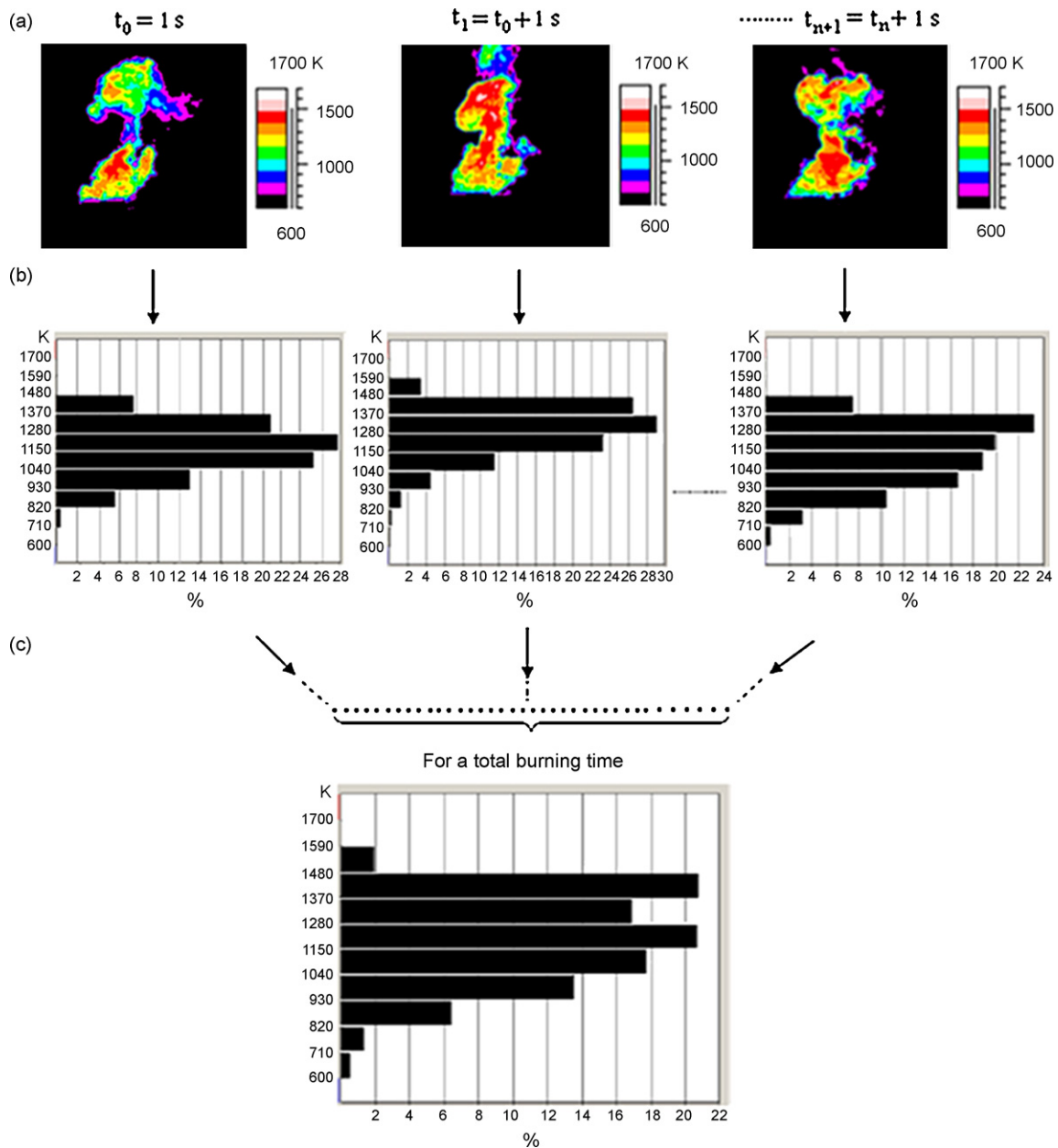
Fig. 2. Evaluation of instantaneous histograms of temperature (b) and time averaged histograms over the total burning time (c) from thermograms (a).

(d = 3.4 m) = 2.70 kg/s) [20]. It is assumed that the fuel is already evaporated and the fuel vapor is coming through the inlet boundary surface to the domain. The mass flow rate used in CFD simulation is determined from the experimental mass burning rate $\overline{\dot{m}}''_f =$ 0.3 kg/(m^2 s) for DTBP pool fires (d = 1.12 and 3.4 m) [20].

The inlet boundary area is surrounded with a low rim (h_{rim} = 0.025 m for d = 1.12 m and h_{rim} = 0.1 m for d = 3.4 m) and an adiabatic ground area. The remaining boundary areas are open boundaries with defined mass fraction of air ($f_{m,air}$ = 1) at ambient conditions (T_a = 293 K and p_a = 1.013 bar).

A non-uniform mesh is used in simulations with the resolution depending on pool diameter: 0.35 × 10^6 cells in the case of the DTBP pool fire with d = 1.12 m and 0.25 × 10^6 cells in the case of d = 3.4 m. The minimum cell size is found near the inlet boundary surface and is 0.022 m in the case of 0.35 × 10^6 cells and 0.06 m in the case of 0.25 × 10^6 cells. The cell size gradually increases with increasing vertical distance from the pool where cells reach the maximum length of 0.55 m in the case of 0.35 × 10^6 cells and 2.6 m in the case

of 0.25 × 10^6 cells. The time steps depend on the pool diameter and the number of cells: t = 10^{-5} s for 0.35 × 10^6 cells and t = 10^{-2} s for 0.25 × 10^6 cells. The number of iterations per time step is 5–10 and gives a sufficient convergence.

The CFD simulation is started at t_0 = 0 with a k–ε turbulence model with a buoyancy correction term [41,42] to reach a certain height of the flame. At t = 10 s the flame is developed and for t > 10 s during a burning time of t_b = 10 s a further simulation of a flame is performed by using scale adaptive simulation (SAS). The burning time t_b starts at 10 s when the flame is developed and ends at 20 s limited by the CPU time. This means that the flame during the burning time of 10 s show a real burning. SAS [41,43] is a hybrid model contains the unsteady Reynolds averaged Navier Stokes equation (URANS) and the large eddy simulation (LES), where URANS acts in the near of wall boundaries and LES in the remaining part of the domain. SAS is an improved URANS formulation, which allows the resolution of the turbulent spectrum in unstable flow conditions. SAS model dynamically adjusts to resolved structures in a URANS
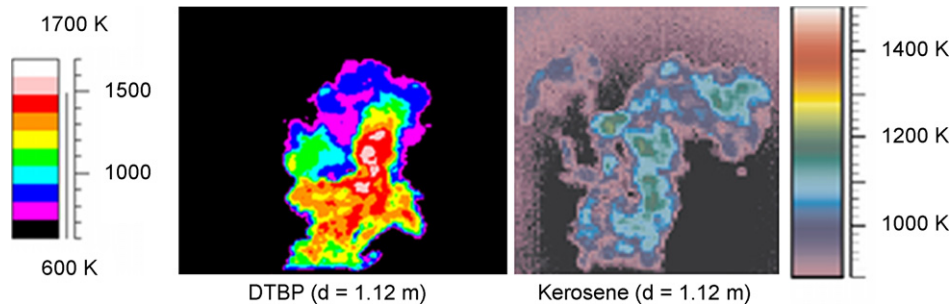
Fig. 3. Instantaneous thermograms of the DTBP (left) and kerosene (right) pool fire with $d = 1.12$ m, measured by a thermographic camera.

simulation, which results in a LES-like behavior in unsteady regions of the flow field. At the same time, the model provides standard RANS capabilities in stable flow regions. The Eddy Dissipation combustion model extended with the Magnussen soot model is used to calculate gas combustion and the formation and combustion of soot [41,44]. A single step overall chemical reaction (stoichiometric combustion) $2C_8H_{18}O_2 + 23O_2 \rightarrow 18H_2O + 16CO_2$ assumes that the fuel is burned with air in one step and lead to the unique products CO_2 and H_2O. For thermal radiation calculation a discrete transfer radiation model (DTM) is used [41].

The coupling between radiation and soot includes an absorption coefficient of the fire. The absorption coefficient k of a DTBP pool fire depends on the volume fraction of soot $f_{v,s}$ and its optical properties and is defined as $k = k_g + k_{m,s}$ with $k_{m,s} = 1226\,f_{v,s}T$ [45,46]. The soot volume fraction $f_{v,s}$ is calculated by using step function of max(0, $f_{m,s}$) in the equation:

$$f_{v,s} = \frac{\max(0, f_{m,s})}{\rho_s}\rho_f \qquad (4)$$

The software package ANSYS CFX-11 is used for the CFD simulations of DTBP pool fires [41].

4. Results and discussion

4.1. Flame temperature

The instantaneous thermograms from a flame consist of a matrix with 640 columns and 480 rows where $T_{i,j}$ is a emission temperature of a pixel element at the position (i, j) [20,22,24].

A series of thermograms of a DTBP pool fire ($d = 1.12$ m) are presented in Fig. 2a and two instantaneous thermograms of a DTBP and a kerosene pool fire are shown in Fig. 3. All pixels with temperatures $T_{i,j} < 600$ K are not considered because regions of these temperatures do not make a significant contribution to the thermal radiation of a pool fire.

The instantaneous temperature distributions of a DTBP pool fire can be presented by histograms determined from instantaneous thermograms (Fig. 2b).

Similar flame inhomogeneities and fluctuations are predicted by CFD, presented in Fig. 4 for a time series.

The time averaged flame temperatures $\bar{T}_{i,j}$ are obtained from a series of thermograms by using the instantaneous temperatures $T_{i,j}$ [24]:

$$\bar{T}_{i,j} = \frac{\sum_i^{N_T} T_{i,j}}{N_T} \qquad (5)$$

The time-averaged histogram (Fig. 2c) obtained by averaging the thermograms with the number N_T shows a large frequency in the range of $1040\,\text{K} \leq T \leq 1480\,\text{K}$ [20].

From each instantaneous thermogram showing a distribution of emission temperatures the maximum centerline temperature profile $T_{i,j,\max}(x)$ is determined. The time averaged maximum flame

temperature $\bar{T}_{i,j,\max}$ is obtained by averaging $T_{i,j,\max}$ over a series of instantaneous thermograms. In the following it is set $\bar{T}_{i,j,\max} = \bar{T}_{\max}$. The measured and predicted centerline profiles of maximum temperatures $\bar{T}_{\max}(x/d)$ of DTBP pool fires are presented in Fig. 5a and b. The $\bar{T}_{CFD}(x/d)$ profiles for $d = 1.12$ m are in good agreement with experimental flame temperature profiles for $x/d > 0.9$. In the lower region of the flame ($x/d < 0.9$), a deviation from the simulated $\bar{T}_{CFD}(x/d)$ exists of up to ≈ 200 K. The predicted maximum temperatures $\bar{T}_{CFD}(x/d = 1.4) = 1440$ K for DTBP pool fires with $d = 3.4$ m is lower than the $\bar{T}_{\max}(x/d \approx 1.3) = 1560$ K [20]. The reason for this difference is probably the use of a single step overall chemical reaction for the DTBP combustion. A flamelet model for the combustion of DTBP is in development.

The $\bar{T}_{exp}$ for various liquid pool fires, measured by Hagglund, Persson, Alger [4] and BAM [20] are summarized in Table 3. The $\bar{T}_{exp}$ of DTBP pool fire ($d = 1.12$ m) is up to 280 K higher than the $\bar{T}_{exp}$ of kerosene, JP-4 and gasoline pool fires at the same d. In a DTBP pool fire ($d = 3.4$ m) the temperature is up to 380 K higher than in JP-4 and gasoline pool fires at the same d.

The reason for the higher temperature in a DTBP fire is the much higher mass burning rate and in addition the released decomposition energy. The –O–O– bond is less stable than the chemical –C–C– bond of hydrocarbons as e.g. in kerosene. Therefore the DTBP molecules decay in the flame. High temperatures ($1500\,\text{K} \lesssim \bar{T} \lesssim 1600\,\text{K}$) in the DTBP pool fires lead to a faster oxidation of soot [46,48] which decreases the soot concentration in these fires.

In kerosene pool fire a relatively large amount of soot is produced which leads to an increase of thermal radiation to the surroundings and therefore to an increase of the emission temperature. However, this increase of the emission temperature is partially compensated by the smoke blockage effect occurring in the most of hydrocarbon pool fires, which leads to a certain decrease of thermal radiation and therefore to a decrease of the emission temperature [24]. The expected much higher temperatures in a less sooty, non-smoky DTBP pool fire than in hydrocarbon pool fires, e.g. kerosene pool fire are not measured because dissociation processes lead to an increasing number of radicals [47,48]. Therefore, the really measured temperature in a DTBP pool fire is to a certain amount lower than the expected high temperature. The emission temperatures in DTBP pool fires can be explained qualitatively by considering some details in chemical reaction mechanisms.

4.2. Surface emissive power (SEP)

In this study the SEP is determined by evaluation of the thermograms which are measured by using a thermographic camera. From instantaneous temperatures $T_{i,j}$ in each pixel element i, j of the thermogram the instantaneous $SEP_{i,j}$ is determined by using the Stefan–Boltzmann-law:

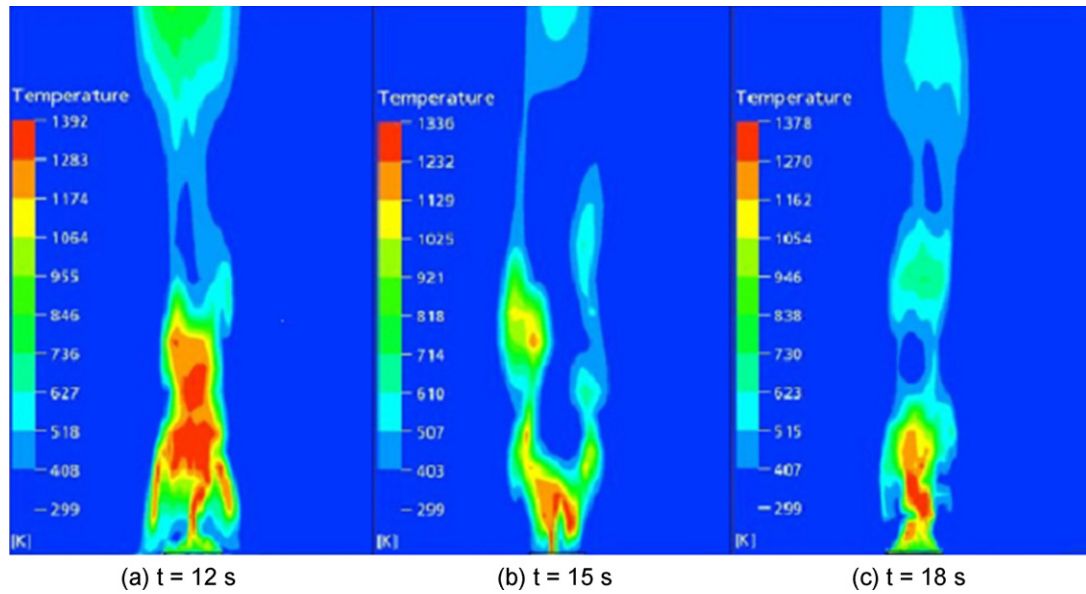$$SEP_{i,j} = \varepsilon_F \sigma T_{i,j}^4 \qquad (6)$$

Fig. 4. CFD predicted sequence of instantaneous flame isotherms of a DTBP pool fire (d = 1.12 m) at different times: (a) t = 12 s, (b) t = 15 s and (c) t = 18 s.

The time and spatial averaged surface emissive power $\overline{SEP}$ is determined by the following equations [22,24]:

$$\overline{SEP} \equiv \langle \overline{SEP}_{i,j} \rangle = \frac{\sum_i \sum_j \overline{SEP}_{i,j} a_x}{\sum_i \sum_j a_x} \tag{7}$$

where

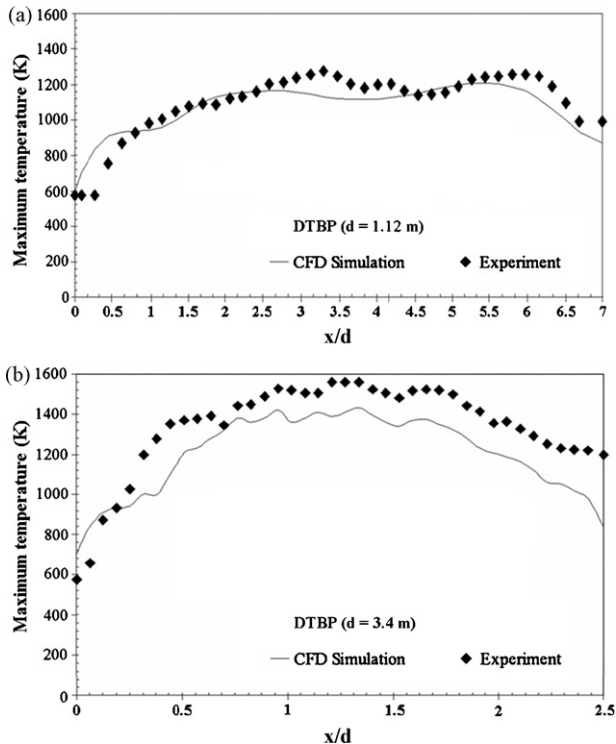$$\overline{SEP}_{i,j} = \frac{\sum_i^{N_T} SEP_{i,j}}{N_T} \tag{8}$$

Fig. 5. Profiles of CFD predicted and measured time averaged centerline maximum emission temperatures $\bar{T}_{max,CFD}(x/d)$, $\bar{T}_{max,exp}(x/d)$ of DTBP pool fires for (a) d = 1.12 m and (b) d = 3.4 m.

In Table 4, $\overline{SEP}$ values of various liquid fuels are presented. The maximum value of $\overline{SEP}_{exp}$ for DTBP pool fires with d = 1.12 m and d = 3.4 m is up to about four times greater than $\overline{SEP}_{exp}$ of gasoline pool fires in the range 1 m $\leq d \leq$ 10 m. The measured surface emissive power for d = 1.12 m and d = 3.4 m is $\overline{SEP}_{DTBP,exp}$ = 130 kW/m² and 250 kW/ m². The $\overline{SEP}_{DTBP,exp}$ (d = 3.4 m) is much higher than the $\overline{SEP}_{exp}$ of hydrocarbon pool fires with the same pool diameter (Fig. 6) [20]. This effect can be explained with the higher emission temperatures and consequently a very low soot concentration in the DTBP pool fires.

In the CFD simulation SEP is predicted via the incident radiation G onto isosurface $A_{F,CFD}$ or in more detail, dG onto infinitesimal surface dA of every cell volume dV, placed on the $A_{F,CFD}$ which represents a real 3D flame surface.

The incident radiation G [24,41,49] is given by

$$G = \frac{1}{A} \int_0^{A_{F,CFD}} G \, dA \tag{9a}$$

$$G = \int_{4\pi \, sr} I(\mathbf{s}) \, d\Omega \tag{9b}$$

$$G(A_{F,CFD}, t) \equiv SEP(A_{F,CFD}, t) \tag{9c}$$

Table 3
Measured time averaged emission temperatures $\bar{T}$ of various pool fires [4,20].

Fuel	d (m)	$\bar{T}$ (K)	Comments
LNG	8.5–15	1500	Estimated using narrow angle radiometer data and spectral data
Gasoline	1–10	1240	
JP-4	0.1–10	1200	
JP-4	7.6–15.2	1400	The maximum temperature at the flame centerline
DTBP[a]	1.12 and 3.4	1480 and 1580	The maximum temperature from thermograms
Kerosene[a]	1.12	1240	The maximum temperature from thermograms

[a] Measured by BAM.

Table 4
Measured time and spatial averaged surface emissive power ($\overline{SEP}$) of various liquid pool fires [4,20].

Fuel	d (m)	$\overline{SEP}$ (kW/m^2)	Comments
LNG	8.5–15	210–280	Estimated using narrow angle radiometer data and spectral data
LNG	1 and 4	20 and 50	
Gasoline	1–10	130–60	Obtained by the maximum temperature from thermograms
Gasoline	2.5	110	
JP-5	30	30	
Kerosene	30–80	10–25	Estimated using wide-angle radiometer data
JP-4	1	100	
JP-5	1	50	
n-Hexane	1	25	
n-Pentane	1 and 2.5	60 and 126	
DTBP[a]	1.12 and 3.4	130 and 250	Obtained by the maximum temperature from thermograms

[a] Measured by BAM.

The radiation intensity I in Eq. (10) is a result of the radiation transport equation [24,41,49]:

$$\frac{dI(\boldsymbol{s})}{ds} = kI_B - kI(\boldsymbol{s}) \tag{10}$$

$$I_B = \frac{\sigma T^4}{\pi\,\mathrm{sr}} \tag{11}$$

The differential Eq. (10) presents the change in I through an absorbing and emitting gray medium along a path length ds in a solid angle Ω defined around the direction of propagation $\boldsymbol{s}$ [24,41,49].

In the CFD simulation of this study the SEP is predicted in three different ways: by determining the flame surface area A_F, axial profile $SEP(x)$ and by integration of G.

In a first way it is necessary to determine the cells lying on a defined isosurface. The following procedure is used to predict the SEP with CFD:

Fig. 6. Measured and CFD predicted $\overline{SEP}$ of DTBP pool fires and other fuels as a function of d.

- An instantaneous flame surface $A_{F,CFD}$ is defined as an isosurface of constant flame temperature T (for DTBP pool fire $T = 1060$ K is used [50]).
- The CFD calculated $G(t)$ is averaged over the isosurface $A_{F,CFD}$ for each time interval Δt (an usually value is $\Delta t = 0.1$ s) to predict instantaneous area averaged $\langle G(t)\rangle$.
- The $\langle G(t)\rangle$ is averaged over a burning time of $t_b = 10$ s which results also in time averaged $\langle \bar{G}\rangle \equiv \overline{SEP}_{CFD}$.

In a second way the $\overline{SEP}_{CFD}$ is determined by averaging along the flame axis up to the height $x = 8$ m for each time step and over the whole burning time of $t_b = 10$ s. The predicted $\overline{SEP}_{DTBP,CFD}$ ($d = 1.12$ m) agree relatively well with the experimentally obtained $\overline{SEP}_{DTBP,exp}$ (Fig. 6). However for $d = 3.4$ m the CFD simulation under predicts the measured $\overline{SEP}_{DTBP,exp}$ by a factor of ≈ 0.72 (Fig. 6). The reason for the lower $\overline{SEP}_{DTBP,CFD}$ values compared with $\overline{SEP}_{DTBP,exp}$ can be caused by using the simplified chemical reaction mechanism. In addition, it should be mentioned that the mesh in the case of DTBP pool fire with $d = 3.4$ m was less fine compared with the mesh for $d = 1.12$ m so that the fine turbulence structures of the small eddies cannot be resolved. In a third way an integration of instantaneous $G(t)$ distribution along the z-direction perpendicular to the x,y-plane is carried out as described in [24].

4.3. Irradiance

In the CFD study virtual radiometers are defined in points placed at different relative distances $\Delta y/d$ from the pool rim as in the experiments [20]. For each virtual radiometer a view factor is defined. A net radiation flux from the flame is received in a certain computational cell where the virtual radiometer is defined. Time
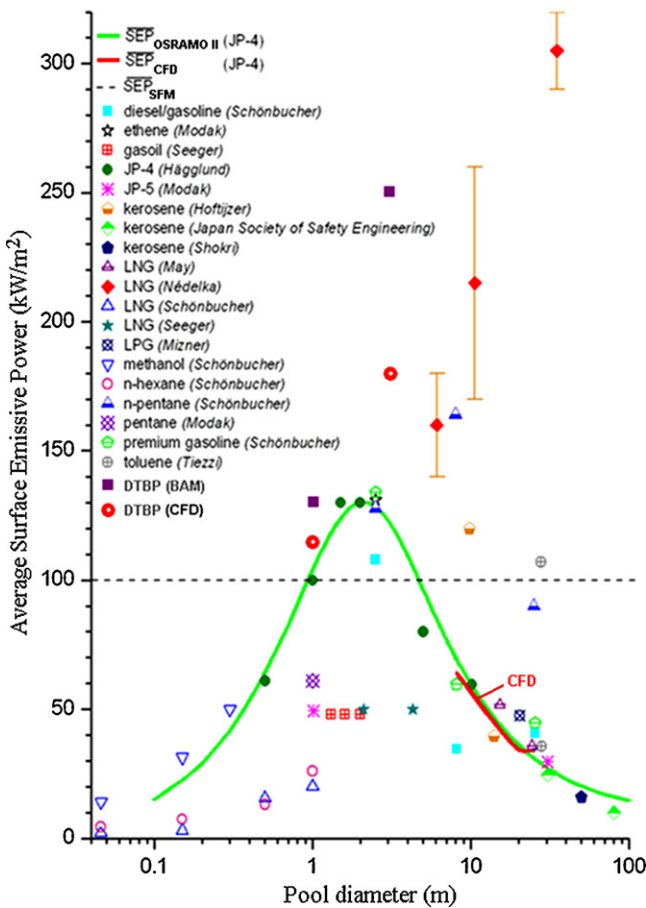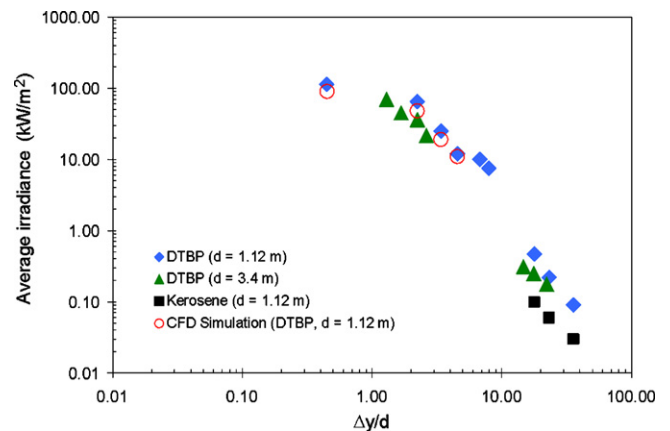

Fig. 7. Measured $\bar{E}_{exp}(\Delta y/d)$ and CFD predicted time averaged irradiances $\bar{E}_{CFD}(\Delta y/d)$ from large-scale DTBP and kerosene pool fires as a function of relative distance $\Delta y/d$ from the pool rim.

dependent irradiances $E_{CFD}(t)$ are averaged over the burning time of $t_b = 10$ s and the time-averaged irradiances $\bar{E}_{CFD}$ are obtained.

Irradiances $\bar{E}(\Delta y/d)$ are measured at different relative distances $\Delta y/d$ from the pool rim for DTBP ($d = 1.12$ and 3.4 m) and kerosene ($d = 1.12$ m) pool fires [20].

The measured averaged irradiances $\bar{E}_{exp}(\Delta y/d)$ of different fires decrease with $\Delta y/d$ (Fig. 7). The $\bar{E}_{exp}$ from DTBP fires are 4–5 times greater than those from kerosene pool fires. The higher temperature and the less soot generation in the DTBP pool fires can explain this effect.

The CFD predicted irradiances $\bar{E}_{exp}(\Delta y/d)$ are in very good agreement with the measured $\bar{E}_{exp}(\Delta y/d)$ at the same distances (Fig. 7). Due to the limited extension of the computational mesh $\bar{E}_{CFD}(\Delta y/d)$ are not calculated for larger distances $\Delta y/d > 4.5$.

5. Conclusions

The following conclusions are summarized from the results:

1. In the case of DTBP pool fires the time-averaged temperatures are up to 380 K higher than for kerosene, JP-4 and gasoline pool fires at the same pool diameter. Opposite to the kerosene pool fire in the DTBP pool fire occurs no smoke layer leading to an increase of surface emissive power and therefore to an increase of the emission temperature.

2. By CFD simulation it is possible to predict the $\overline{SEP}_{CFD}$ of the flame. It is necessary to define a flame surface. In this study the surface is defined as an isosurface $A_{F,CFD}$ of a constant flame temperature, here the time averaged temperature of hot spots. The predicted $\overline{SEP}_{CFD}$ is than in a good agreement with $\overline{SEP}_{exp}$. Also by determining the time and space averaged centerline profiles the $\overline{SEP}_{exp}$ can be predicted. With the CFD simulation it is also possible to predict time dependent irradiances $E_{CFD}(\Delta y/d, t)$ and time averaged $\bar{E}_{CFD}(\Delta y/d)$ by defining virtual radiometers at the pool rim and at different horizontal distances $\Delta y/d$ from the pool rim.

3. The presented CFD simulation is a first step to predict the thermal radiation from accidental DTBP pool fires to neighboring plants and people.

References

[1] The Buncefield Investigation, Progress Report, February 2006, www.buncefieldinvestigation.gov.uk/report.pdf.

[2] D.S. Burgess, A. Strasser, J. Grumer, Diffusive burning of liquid fuels in open trays, Fire Res. Abstr. Rev. 3 (1961) 177–192.

[3] A. Schönbucher, W. Brötz, C. Balluff, D. Göck, N. Schieß, Erforschung von Schadenfeuern flüssiger Kohlenwasserstoffe in: Sicherheit von Chemieanlagen, Chem. Ing. Tech. 57 (1985) 823–834.

[4] K.S. Mudan, Thermal radiation hazards from hydrocarbon pool fires, Prog. Energy Comb. Sci. 10 (1984) 59–80.

[5] M.S. Mannan, Lee's Loss Prevention in the Process Industries, vols. 1–3, 3rd edition, Elsevier Butterworth-Heinemann, Burlington, Massachusetts, 2005.

[6] T.A. Roberts, R. Merrifield, S. Tharmalingam, Thermal radiation hazards from organic peroxides, J. Loss Prev. Process Ind. 3 (1990) 244–252.

[7] M. Gawlowski, M. Hailwood, I. Vela, A. Schönbucher, Deterministic and probabilistic estimation of appropriate distances: motivation for considering the consequences for industrial sites, Chem. Eng. Technol. (2009), doi:10.1002/ceat.200800631.

[8] C.L. Beyler, Fire hazard calculations for large, open hydrocarbon fires, in: The SFPE Handbook of Fire Protection Engineering, 3rd ed., National Fire Protection Association, Quincy, MA, 2002, Section 3, Chapter 11, pp. 3–268.

[9] T. Steinhaus, S. Welch, R. Carvel, J.L. Torero, Large-scale pool fires, Therm. Sci. J. 11 (3) (2007) 101–118.

[10] S.R. Tieszen, On the fluid mechanic in fires, Annu. Rev. Fluid Mech. 33 (2001) 67–92, doi:10.1146/annurev.fluid.33.1.67.

[11] H. Koseki, Scale dependency of radiation and smoke emission from large pool fires, in: Proceeding of the 2nd International Symposium on Scale Modeling, 1997, p. 87.

[12] A. Hamins, T. Kashiwagi, R.R. Burch, Fire resistance of industrial fluids, in: G.E. Totten, J. Reichel (Eds.), Proceedings of the ASTM STP 1284, Indianapolis, ASTM, Philadelphia, June 20, 1995, 1996, pp. 15–41.

[13] H. Koseki, Y. Iwata, Tomakomai large scale crude oil fire experiments, Fire Technol. 36 (1) (2000) 24–38.

[14] P. Joulain, The behaviour of pool fires: state of the art and new insights, in: Proceedings of the 27th International Symposium on Combustion, The Combustion Institute, 1998, pp. 2691–2706.

[15] M. Hertzberg, The theory of free ambient fires. The convectively mixed combustion of fuel reservoirs, Combust. Flame 21 (1973) 195–209.

[16] M. Shokri, C.L. Beyler, Radiation from large pool fires, J. Fire Prot. Eng. 1 (4) (1989) 141–150.

[17] Th.M. Groothuizen, J. Romjin, Heat radiation from fires of organic peroxides as compared with propellant fires, J. Hazard. Mater. 1 (1975/76) 191–198.

[18] K.-D. Wehrstedt, P.-A. Wandrey, Burning behaviors of explosive liquid substances as a function of pool diameter, Report No. PTB-W-54, PTB, 1993, pp. 97–108.

[19] Y. Iizuka, M. Surianarayanan, Comprehensive kinetic model for adiabatic decomposition of di-tert-butyl peroxide using batch CAD, Ind. Eng. Chem. Res. 42 (2003) 2987–2995.

[20] H. Chun, Experimentelle Untersuchungen und CFD-Simulation von DTBP-Poolfeuern, BAM-Dissertationsreihe, Band 23, Berlin, 2007, www.bam.de/de/service/publikationen/publikationen_medien/diss_23_vt.pdf.

[21] Safety report assessment guide: chemical warehouses – hazards, in: SRAG—Chemical Warehouses, Version 6, June 26, 2002, www.hse.gov.uk/comah/sragcwh/hazards/haz5.htm.

[22] M. Munoz, J. Arnaldos, J. Casal, E. Planas, Analysis of the geometric and radiative characteristics of hydrocarbon pool fires, Combust. Flame 139 (2004) 263–277.

[23] M. Munoz, E. Planas, F. Ferrero, J. Casal, Predicting the emissive power of hydrocarbon pool fires, J. Hazard. Mater. 144 (2007) 725–729.

[24] I. Vela, H. Chun, M. Gawlowski, K.B. Mishra, P. Sudhoff, K.-D. Wehrstedt, A. Schönbucher, Vorhersage der thermischen Strahlung großer Kohlenwasserstoff- und Peroxid-Poolfeuer durch CFD Simulation, Chem. Ing. Tech. 81 (1–2) (2009), in press.

[25] J.A. Fay, Model of large pool fires, J. Hazard. Mater. B 136 (2006) 219–232.

[26] P.K. Raj, Large hydrocarbon fuel pool fires: physical characteristics and thermal emission variation with heights, J. Hazard. Mater. 5 (1981) 111.

[27] P.J. Rew, W.G. Hulbert, D.M. Deaves, Modeling of thermal radiation from external hydrocarbon pool fires, Trans. IChemE. 75 (Part B) (1997) 81–89.

[28] K.S. Mudan, P.A. Croce, Fire hazard calculations for large open hydrocarbon fires, in: The SFPE Handbook of Fire Protection Engineering, First edition, NFPA, Quincy, MA, USA, 1988, Section 2, Chapter 4.

[29] C.J.H. van den Bosch, R.A.P.M. Weterings, Methods for the calculation of physical effects, in: Yellow Book, 3rd ed., CPR 14E, Heat flux from fires, 6.1-6.130, 1997, ISBN: 9012084970, Part 2, Chapter 6.

[30] K.B. McGrattan, H.R. Baum, R.G. Rehm, Large eddy simulations of smoke movement, Fire Saf. J. 30 (1998) 161–178.

[31] F.P. Lees, in: S. Mannan (Ed.), Loss Prevention in the Process Industries, vol. 2, 3rd ed., Elsevier Butterworth-Heinmann, Burlington, MA, 2005.

[32] V. Novozhilov, H. Koseki, Computational fluid dynamics prediction of self-sustained pool fire combustion, J. Inst. Eng., Singapore 1 (5) (2004) 69–82.

[33] T.C. Henderson, P.A. McMurtry, P.J. Smith, G.A. Voth, C.A. Wight, D.F. Pershing, Simulating accidental fires and explosions, Comput. Sci. Eng. 2 (2) (2000) 64–76.

[34] J.P. Spinti, J.N. Thornock, E.G. Eddings, P.J. Smith, A.F. Sarofim, Heat transfer to object in pool fires, in: Proceedings of the Combustion Institute, vol. 29, Issue 1, 2002, pp. 259–266.

[35] M. Greiner, A. Suo-Anttila, Radiation heat transfer and reaction chemistry models for risk assessment compatible fire simulations, J. Fire Protect. Eng. 16 (2) (2006) 79–103.

[36] M. Greiner, A. Suo-Anttila, Validation of the Isis-3D computer code for simulating large pool fires under a variety of wind conditions, J. Pressure Vessel Technol. 126 (2004) 360–368.

[37] Y.L. Sinai, Exploratory CFD modelling of pool fire instabilities without cross-wind, Fire Saf. J. 35 (2000) 51–61.

[38] H. Baum, Large eddy simulation of fires, Fire Protect. Eng. (2000) 36–42.

[39] V.F. Nicolette, L.A. Gritzo, Comparison of the KAMELEON fire model to large-scale open pool fire data, Thermal & fluid engineering, Proceedings of the 4th International Symposium on Fire Safety Science 1994, Report SAND-93-2416C; CONF-940668-3.

[40] E. Planas-Cuchi, J.M. Chatris, C. Lopez, J. Arnaldos, Determination of flame emissivity in hydrocarbon pool fires using infrared thermography, Fire Technol. 39 (2003) 261–273.

[41] ANSYS CFX 11.0 User Guide, AEA Technology, 2007, www.ansys.com.
[42] B.E. Launder, W. Rodi, Progress in development of Reynolds-stress, Fluid Mech. 68 (1975) 537–566.
[43] F. Menter, Y. Egorov, A scale adaptive simulation model using two-equation models, ANSYS CFX, Otterfing, Germany AIAA-2005–1095, 43rd AIAA Aerospace Sciences Meeting and Exhibit, Reno, Nevada, January 10–13, 2005.
[44] B.F. Magnussen, B.H. Hjertager, On mathematical modeling of turbulent combustion with special emphasis on soot formation and combustion, in: Proceedings of the 16th International Symposium on Combustion, The Combustion Institute, 1976, pp. 719–729.
[45] R.J. Goldstein, E.R.G. Eckert, W.E. Ibele, S.V. Patankar, T.W. Simon, T.H. Kuehn, P.J. Strykowski, K.K. Tamma, J.V.R. Heberlein, J.H. Davidson, J. Bischof, F.A. Kulacki, U. Kortshagen, S. Garrick, Heat transfer—a review of 2001 literature, Int. J. Heat Mass Transfer 46 (2003) 1887–1992.

[46] C. Lautenberger, J. de Ris, N. Dembsey, A simplified model for soot formation and oxidation in CFD simulation of non-premixed hydrocarbon flames, Fire Saf. J. 40 (2005) 141–176.
[47] J. Warnatz, U. Mass, R.W. Dibble, Combustion, Physical and Chemical Fundamentals, Modeling and Simulation, Experiments, Pollutant Formation, 4th ed., Springer–Verlag, New York, 2006, ISBN 3-540-25992-9.
[48] H. Steen, Handbuch des Explosionsschutzes, Wiley-VCH Verlag GmbH, D-69469 Weinheim, 2000, ISBN 3-527-29848-7.
[49] K.A. Jensen, J.-F. Ripoll, A.A. Wray, D. Joseph, M. El Hafi, On various modeling approaches to radiative heat transfer in pool fires, Combust. Flame 148 (2007) 263–279.
[50] M. Gawlowski, M. Hailwood, B. Schalau, A. Schönbucher, Conclusions drawn from the Buncefield and Naples incidents regarding the utilization of consequence models, Chem. Eng. Technol. (2009), doi:10.1002/ceat.200800595.